

3D effects of neon injection positions on the toroidally symmetric/asymmetric heat flux distribution on EAST

journal or publication title	Plasma Physics and Controlled Fusion
volume	62
number	3
page range	035003
year	2020-01-14
URL	http://hdl.handle.net/10655/00012802

doi: 10.1088/1361-6587/ab6072



3D effects of neon injection position on the toroidally symmetric/asymmetric heat flux distribution on EAST

B. Liu^{1,*}, S.Y. Dai^{1,*}, G. Kawamura^{2,3}, L. Zhang⁴, Y. Feng⁵ and D.Z. Wang¹

¹*Key Laboratory of Materials Modification by Laser, Ion and Electron Beams (Ministry of Education), School of Physics, Dalian University of Technology, Dalian 116024, China*

²*National Institute for Fusion Science, National Institutes of Natural Sciences, Toki 509-5292, Japan*

³*Department of Fusion Science, the Graduate University for Advanced Studies, SOKENDAI, Toki 509-5292, Japan*

⁴*Institute of Plasma Physics, Chinese Academy of Sciences, Hefei 230031, People's Republic of China*

⁵*Max-Planck-Institut für Plasmaphysik, D-17491 Greifswald, Germany*

Email: daishuyu@dlut.edu.cn

Abstract

The heat flux deposition on the divertor targets with neon impurity injection on EAST has been investigated by the three-dimensional (3D) edge transport code EMC3-EIRENE. Impact of the different poloidal neon injection positions on heat flux deposition has been studied. It is found that neon impurity injected at the in- and out-board divertors (i.e. strike points) leads to the toroidally asymmetric distributions of heat load on the in- and out-board targets, respectively. However, the neon gas puffing at the upstream shows a toroidally symmetric distribution of heat load. The 3D effects of the neon radiation on the heat load have been investigated with the help of a field line tracing technique, which indicates that neon impurity injected near the strike point can radiate more power and result in a lower heat load compared with the upstream neon injection. In order to further verify the asymmetric distribution of heat load, two impurity injection locations away from the strike points at the divertor are investigated, which shows the symmetric distribution of heat load as the upstream neon injection.

Keywords: heat flux deposition, neon impurity, EAST

* These authors contributed equally to this work and should be considered co-first authors.

1. Introduction

One of the most critical issues in fusion devices is mitigation of the heat flux deposition on the plasma-facing components (PFCs) [1,2]. The methods of heat flux mitigation on PFCs have emerged such as resonant magnetic perturbations [3] and advanced divertor geometry [4-6]. The extrinsic impurity seeding is also utilized to achieve the power dissipation and heat load reduction in existing fusion facilities. The effect of gas puffing with neon, nitrogen and argon has been investigated on Alcator C-Mod [7], JET [8], LHD [9] and EAST [10]. On Alcator C-Mod, with localized nitrogen injection in the private flux region, an asymmetric toroidal distribution of radiation power and heat load on PFCs is observed [11,12]. Experiments and simulations on LHD also show that a toroidally non-uniform distribution of heat load is obtained for nitrogen impurity seeding, while a toroidally uniform distribution of heat load is achieved for neon impurity seeding [13]. The symmetric (neon) and asymmetric (nitrogen) heat flux distributions observed on Alcator C-Mod and LHD result from different recycling characteristics for neon (high recycling) and nitrogen (low recycling) [11-13]. However, influence of the poloidal impurity injection on the toroidally symmetric/asymmetric distributions of heat load on the divertor targets is not well understood. Hence, predictive modelling of heat flux distributions with different poloidal gas injection positions is important for understanding the mechanisms in order to optimize impurity puffing position for heat load mitigation in fusion devices.

In this work, impact of different poloidal neon impurity injections on the toroidal distributions of heat flux deposition on EAST is studied with the help of 3D edge transport code EMC3-EIRENE [14,15]. The EMC3-EIRENE code has the availability of 3D magnetic configuration reconstruction, which allows to study the 3D effects of spatial impurity transport and radiation on the divertor heat flux distribution. The analysis of the heat flux deposition on the divertor targets at five different poloidal locations with neon seeding is reported. An innovative result is found that neon impurity injections around the in- and out-board strike points lead to the toroidally asymmetric distributions of heat load on the in- and out-board divertor targets, respectively. However, the impurity injection at the upstream results in a toroidally uniform heat flux distribution due to above-mentioned high-recycling property. The field line tracing (FLT) [16-20] technique is used to make a detailed numerical analysis of the relation between 3D neon radiation in scrape-off layer (SOL) and heat flux deposition on the divertor targets. Two impurity injection locations away from the strike point at the divertor were used to verify the distribution of the heat load. The higher impurity radiation power for neon injections near the strike points results in the larger reduction of heat load, in comparison to the injection at an upstream location.

In section 2, the construction of the EMC3-EIRENE simulations is addressed. In section 3, impact of different poloidal neon injection positions on the heat flux deposition distribution is

studied. Furthermore, detailed analysis of 3D neon radiation in SOL and heat load on the divertor targets has been conducted. Finally, a summary is given in section 4.

2. Construction of EMC3-EIRENE simulations

The EMC3-EIRENE code deals with arbitrary magnetic confinement configurations and has been successfully applied to many fusion devices, including W7-AS [21], Alcator C-Mod [7], LHD [22-26], DIII-D [27-30], NSTX [31], ASDEX Upgrade [32-35] and EAST [36-39] etc. The code solves a set of time-independent Braginskii's fluid equations for the mass, momentum and energy for electrons and ions using a Monte Carlo (MC) method [13] and is iteratively coupled with EIRENE [14], that solves the kinetic Boltzmann equation for neutral atoms or molecules and gives the particle momentum and energy source terms due to plasma-neutral interactions. The parallel transport along with field line is assumed to be classical and the cross-field transport is treated as anomalous. The code also includes a self-consistent treatment of impurity transport for investigating relevant impurities [40]. In the impurity transport model, the friction and the ion thermal force are the dominant forces acting on the impurity, where the friction force drives impurity particles to the divertor targets and the ion thermal force propels impurity towards the upstream direction [41].

The EMC3-EIRENE code requires a 3D computational grid that divides the whole computational domain into finite volumes and stores the entire magnetic geometry [42]. In this work, the computational domain of EMC3-EIRENE spans the whole torus (360°) and divides toroidal domains with a toroidal resolution of about 2.8° . The magnetic field aligned grid used by EMC3-EIRENE provides computationally effective access to fast magnetic field reconstruction during the MC particle tracing. The code uses a reversible field line mapping technique for the transport of individual MC particle across the toroidal block boundary [43]. The upper divertor of EAST has been upgraded to tungsten targets since 2014 campaign. Heat flux control on upper tungsten divertor is a critical topic for steady-state and long-term operation on EAST. Hence, the computational grid used in this work is constructed based on an upper single null magnetic configuration plasma discharge denoted by the shot number #74209 during the steady-state period at 4.0s on EAST. A two-dimensional (2D) poloidal cross section of the computational grid is shown in figure 1.

Deuterium is used as the main plasma species with neon as the extrinsic impurity injected into the torus. Five neon injections at Upstream (U0), Inboard Divertor (ID0, ID1) and Outboard Divertor (OD0, OD1) are indicated in figure 1 and table 1. The toroidal location of the neon impurity injection position is initialized as the toroidal angle of $\varphi = 0^\circ$ in this study. The injected neon rate of $6.25 \times 10^{20} \text{ s}^{-1}$ with an initial energy of 0.03 eV is used as an input for all the cases. Due to the low chemical activity of neon, the impurity recycling coefficient of 0.99 is assumed [13]. The simulation assumes a total input power of 2.66 MW, shared equally between electrons and ions

[21,44,45]. The toroidal directions of the plasma current I_p (0.37 MA) and the toroidal magnetic field B_t (2.5 T) are in the anti-clockwise and clockwise directions from top view, respectively. The upstream density of $1.0 \times 10^{19} \text{ m}^{-3}$ is set as the boundary condition for the particle transport. The cross-field transport of particle and heat modelled by the diffusive transport coefficients are set as, $D_{\perp} = 0.4 \text{ m}^2 \text{ s}^{-1}$ and $\chi_{\perp} = 3D_{\perp}$. The impurity perpendicular diffusivity, D_{imp} is assumed to be equal to the perpendicular diffusivity of the background plasma, i.e. $0.4 \text{ m}^2 \text{ s}^{-1}$.

3. Results and discussion

3.1 Neon injections near the divertor strike points and at upstream

3.1.1 Toroidally symmetry/asymmetric distributions of heat load

Figures 2(a-f) show the 2D distributions of heat flux deposition on the upper in- and out-board divertor targets with neon impurity injections at U0, ID0 and OD0. The downstream injections at ID0 and OD0 result in a lower heat flux deposition on the upper in- and out-board divertor targets compared with the upstream injection at U0. The most effective suppression of heat load on the upper inboard divertor targets is achieved with the injection at ID0, resulting in a peak value $\sim 1.2 \text{ MW/m}^2$ (figure 2(b)). Additionally, the neon impurity injections at ID0 and OD0 result in the toroidally asymmetric distributions of heat load on the upper in- and out-board targets (figures 2(b) and (f)), respectively. A reduction in the heat flux magnitude with increase in the toroidal angle, starting from the injection location on the inboard targets is observed in figure 2(b). An obvious suppression in heat load from the toroidal angle of $\varphi = -45^\circ$ to -20° is also obtained on the upper outboard targets in figure 2(f).

Figures 3(a-b) show the poloidal distributions of heat flux along the divertor targets (ID0 injection and no neon case) for the upper in- and out-board divertor targets at toroidal angles of $\varphi = 60^\circ$ and -120° . The peak heat loads on the upper inboard targets are $\sim 0.6 \text{ MW/m}^2$ and 1.1 MW/m^2 at $\varphi = 60^\circ$ and -120° (figure 3(a)), respectively. However, the heat flux distributions on the upper outboard target with injection at ID0 are similar at the toroidal angles of $\varphi = 60^\circ$ and -120° (figure 3(b)), which does not show an asymmetric property of the heat flux distribution as shown in figure 2(e). This indicates that the neon impurity injection around the strike point at the inboard divertor only leads to a toroidally asymmetric distribution of heat load on the inboard targets. For the sake of comparison, the heat flux distribution without the neon injection is also shown in figure 3. The larger heat loads of ~ 2.8 and 3.7 MW/m^2 on the upper in- and out-board targets are obtained for no neon injection case, respectively. Additionally, the poloidal profiles of the heat load for the upper in- and out-board divertor targets (OD0 injection and no neon case) along the divertor targets at the toroidal angles of $\varphi = -30^\circ$ and 150° are compared in figures 3(c-d). The peak values of heat flux deposition on the upper outboard target at the toroidal angles of $\varphi = -30^\circ$ and 150° are

~ 0.8 and 1.75 MW/m^2 (figure 3(d)), respectively. However, no toroidal asymmetry of heat flux profiles is obtained at the toroidal angles of $\varphi = -30^\circ$ and 150° on the upper inboard targets (figure 3(c)). Based on the above simulations, a unique result is found that neon impurity injections near the strike points at the in- and out-board divertors result in the toroidally asymmetric distributions of heat load on the in- and out-board targets, respectively. The detailed analysis of toroidally asymmetric heat load distribution has been performed in the following subsections.

In addition, a parameter study has been performed to examine the sensitivity of the asymmetric distribution of heat load on the upstream electron density in figure 4. The 2D distributions of heat load on the in- and out-board divertor targets are displayed in figure 4 for neon injections at ID0 and OD0 with upstream electron density of 0.8 and $1.2 \times 10^{19} \text{ m}^{-3}$. It is seen that the toroidally asymmetric distributions of heat load on the upper targets can be obtained as well as the case of $1.0 \times 10^{19} \text{ m}^{-3}$. Hence, the toroidal asymmetry of heat load on the divertor targets is associated with the poloidal neon injection position instead of the edge plasma parameters.

3.1.2 3D analysis of toroidally asymmetric heat load for the strike-point injections

The studies of the relation between 3D neon radiation in SOL and heat flux deposition on the divertor targets have been conducted with the help of the FLT approach to make clear the reason for above-mentioned toroidally asymmetric heat load. The start points for FLT are located on the inboard targets at the toroidal angles of $\varphi = 60^\circ$ (P1 in figure 2(b)) and -120° (the opposite toroidal location of P1). The corresponding flux tubes are named FT(60°) and FT(-120°) to facilitate the discussion below. Figures 5(a-d) show the electron density and temperature, neon ions density and radiation power along two flux tubes FT(60°) and FT(-120°). It is seen that the n_e and T_e at the upstream for FT(60°) and FT(-120°) are virtually identical as shown in figures 5(a-b), respectively. This indicates that the incoming powers into FT(60°) and FT(-120°) are same at the upstream. On the other hand, at the downstream divertor region, the neon ions density for FT(60°) is about two orders of magnitude higher than that for FT(-120°) (figure 5(c)), which results in a much larger neon radiation power for FT(60°) compared to that for FT(-120°) (figure 5(d)). As a result, the stronger energy loss for FT(60°) leads to the lower heat load on the divertor targets at P1 (figure 2(b)).

The same analysis for the toroidally asymmetric heat load distribution on the upper outboard targets has been performed in figures 6(a-d). The start points for FLT on the outboard targets are selected at the toroidal angles of $\varphi = -30^\circ$ (P2 in figure 2(f)) and 150° (the opposite toroidal location of P2). The flux tubes are denominated as FT(-30°) and FT(150°), respectively. Figures 6(a-d) display the electron density and temperature, neon ions density and radiation power along the flux tubes FT(-30°) and FT(150°). The same incoming energy into FT(-30°) and FT(150°) is obtained according to the n_e and T_e at the upstream in figures 6(a-b). At the same time, the much higher neon

ions density and radiation power at the divertor region are achieved for FT(-30°), which leads to a lower heat load at P2 (figure 2(f)). Consequently, the same incoming energy at the upstream but different power losses at the divertor region result in the toroidal asymmetry of heat load on the upper in- and out-board targets.

3.1.3 Dependence of toroidally asymmetric heat load on poloidal injection position

The above simulations in figure 2 also demonstrate that the toroidally asymmetric heat load distributions on the in- and out-board targets show a dependence on the poloidal neon injection position. The detailed analysis of the relation between the upstream energy source, power exhaust by neon and resulting heat load for different neon injections at U0, ID0 and OD0 has been conducted by the FLT approach. Figures 7(a-d) show the electron density and temperature, neon ions density and radiation power along the flux tube FT(60°) from P1 on the upper inboard target with different neon injections. The flux tube FT(60°) rotates toroidally (16 turns) from a toroidal angle of 60° to about -6000° and terminates at the outboard divertor target. The upstream n_e and T_e for neon injections at U0, ID0 and OD0 are similar (figures 7(a-b)). However, both the neon ions density and radiation power are much higher at the high field side with the ID0 injection compared to the U0 and OD0 injections (figures 7(c-d)). Therefore, a resulting lower heat load at P1 on the upper inboard target is obtained for the ID0 injection in figure 2(b) in contrast to the U0 and OD0 injections in figures 2(a) and (c).

Further, the FLT from P2 on the upper outboard target has been carried out to study the heat load distribution on the outboard targets with different poloidal neon injection positions. Figures 8(a-d) show the electron density and temperature, neon ions density and radiation power along the flux tube FT(-30°) from P2 on the upper outboard target with different neon injections. Likewise, the higher power exhaust at the low field side for the OD0 injection (figure 8(d)) with the similar incoming energy into FT(-30°) at the upstream according to figures 8(a-b) results in a smaller heat load at P2 on the upper outboard targets in figure 2(f), in comparison with the U0 and ID0 injections in figures 2(d) and (e), respectively.

3.2 Neon injections away from the strike points at the divertor

Based on the above simulations, one can see that the toroidally asymmetric distribution of heat load shows a dependence on the neon injection location. However, it is uncertain that the asymmetry of heat load is induced by neon injection near the strike point or at the downstream divertor compared to the upstream neon injection. Hence, two injection positions named ID1 and OD1 away from the

strike points as shown in figure 1 are used to resolve this issue. Figures 9(a-d) present the 2D distributions of the heat load on the upper in- and out-board targets with neon injections at ID1 and OD1. The toroidally uniform heat load distributions are obtained for both ID1 and OD1 injections. Therefore, it is confirmed that the asymmetry of heat load distribution on the divertor targets is attributed to the neon injection near the strike point instead of that at the downstream divertor.

FLT method is employed to investigate the toroidally asymmetric/symmetric distributions of heat load on the divertor targets with neon injections at ID0/ID1 and OD0/OD1, respectively. Figures 10 and 11 show the electron density and temperature, neon ions density and radiation power for the divertor and upstream injections along the flux tubes FT(60°) and FT(-30°), respectively. The similar n_e and T_e are obtained for neon injections at U0, ID0 and ID1 along the flux tube FT(60°) at the upstream (figures 10(a-b)). However, both the neon ions density and radiation power are much lower with the ID1 injection compared to the ID0 injection (figures 10(c-d)). Therefore, the stronger spatial power exhaust for ID0 injection results in a smaller heat load at P1 on the inboard divertor targets (figure 2(b)), in comparison with the U0 and ID1 injections (figures 2(a) and 9(a)). Likewise, the higher power exhaust for the OD0 injection (figure 11(d)) with the similar incoming energy into FT(-30°) at the upstream according to figures 11(a-b) results in a lower heat load at P2 on the upper outboard targets (figure 2(f)), in contrast to that for the U0 and OD1 injections (figures 2(d) and 9(d)).

4. Summary

The impact of different poloidal neon injection positions on the toroidally symmetric/asymmetric distributions of heat load on the divertor targets has been investigated by EMC3-EIRENE code. It is found that neon injections near the strike points on the in- and out-board divertor targets lead to the toroidally asymmetric heat load distributions on the in- and out-board targets, respectively. The relation between the upstream energy source, downstream neon radiation and resulting heat load on the divertor target has been investigated by means of the field line tracing technique. The neon injections near the strike points lead to a higher radiation power at the divertor region, that results in a lower heat load in contrast to the upstream neon injection. Two neon injections away from the strike points at the divertor are investigated to further confirm the asymmetric distribution of heat load, which shows the symmetric distribution of heat load as the upstream neon injection.

Acknowledgments

This work was supported by National MCF Energy R&D Program of China Nos: 2018YFE0311100, 2018YFE0303105, 2017YFE0300501, 2017YFE0301206 and 2017YFE0300402, National Natural

Science Foundation of China under Grant Nos. 11405021, 11675037, 11575244 and 11775269, High-level talent innovation support program of Dalian No. 2017RQ052, and the Fundamental Research Funds for the Central Universities No. DUT18LK03, and was supported partly by Japan-China Collaboration for Fusion Research (Post-CUP Collaboration) and JSPS KAKENHI Grant Number 16K18340.

References

- [1] Federici G *et al* 2001 *Nucl. Fusion* **41** 1967
- [2] Loarte A *et al* 2007 *Nucl. Fusion* **47** S203
- [3] Schmitz O *et al* 2016 *Nucl. Fusion* **56** 066008
- [4] Ryutov D D *et al* 2007 *Phys. Plasmas* **14** 064502
- [5] Valanju P M *et al* 2009 *Phys. Plasmas* **14** 056110
- [6] Kotschenreuther M *et al* 2007 *Phys. Plasmas* **14** 072502
- [7] Loarte A *et al* 2011 *Phys. Plasmas* **18** 056105
- [8] Oberkofler M *et al* 2013 *J. Nucl. Mater.* **438** S258-261
- [9] Tanaka M *et al* 2017 *Nucl. Mater. Energy* **12** 241
- [10] Chen J B *et al* 2017 *Chin. Phys. B* **26** 095205
- [11] Lore J D *et al* 2015 *Phys. Plasmas* **22** 056106
- [12] Lore J D *et al* 2015 *J. Nucl. Mater.* **463** 515
- [13] Kawamura G *et al* 2018 *Plasma Phys. Control. Fusion* **60** 084005
- [14] Feng Y *et al* 2004 *Contrib. to Plasma Phys.* **44** 57
- [15] Reiter D *et al* 2005 *Fusion Sci. Technol.* **47** 172
- [16] Firdaouss M *et al* 2013 *J. Nucl. Mater.* **438** S536-539
- [17] Kos L *et al* 2019 *Fusion Eng. Des.* **146** 1796-1800
- [18] Arter W *et al* 2014 *IEEE Trans. Plasma Sci.* **42** 1932-1942
- [19] Zhang B *et al* 2016 *Fusion Eng. Des.* **107** 58-63
- [20] Arter W *et al* 2015 *IEEE Trans. Plasma Sci.* **43** 3323-3331
- [21] Feng Y *et al* 1999 *J. Nucl. Mater.* **266-269** 812
- [22] Dai S Y *et al* 2017 *Plasma Phys. Control. Fusion* **59** 085013
- [23] Dai S Y *et al* 2018 *Nucl. Fusion* **58** 096024
- [24] Dai S Y *et al* 2016 *Nucl. Fusion* **56** 066005
- [25] Kobayashi M *et al* 2013 *Nucl. Fusion* **53** 033011
- [26] Kawamura G *et al* 2014 *Contrib. to Plasma Phys.* **54** 437
- [27] Lore J D *et al* 2017 *Nucl. Fusion* **57** 056025
- [28] Frerichs H *et al* 2014 *Phys. Plasmas* **21** 020702
- [29] Frerichs H *et al* 2015 *Phys. Plasmas* **22** 072508

- [30] Frerichs H *et al* 2012 *Nucl. Fusion* **52** 054008
- [31] Lore J D *et al* 2012 *Nucl. Fusion* **52** 054012
- [32] Brida D *et al* 2017 *Nucl. Fusion* **57** 116006
- [33] Lunt T *et al* 2012 *Nucl. Fusion* **52** 054013
- [34] Zhang W *et al* 2016 *Nucl. Fusion* **56** 036007
- [35] Lunt T *et al* 2011 *J. Nucl. Mater.* **415** S505-8
- [36] Xie T *et al* 2018 *Nucl. Fusion* **58** 106017
- [37] Huang J *et al* 2014 *Plasma Phys. Control. Fusion* **56** 075023
- [38] Xie T *et al* 2018 *Fusion Eng. Des.* **136** 699-705
- [39] Xu S *et al* 2018 *Nucl. Fusion* **58** 106008
- [40] Feng Y *et al* 2002 *Plasma Phys. Control. Fusion* **44** 611
- [41] Stangeby P.C. 2000 *The Plasma Boundary of Magnetic Fusion Devices* (Bristol: Institute of Physics Publishing)
- [42] Lunt T *et al* 2011 *Plasma Phys. Control. Fusion* **53** 125010
- [43] Feng Y *et al* 2005 *Phys. Plasmas* **12** 052505
- [44] Feng Y *et al* 2017 *Plasma Phys. Control. Fusion* **59** 034006
- [45] Feng Y *et al* 2006 *Nucl. Fusion* **46** 807-819

Figure captions:

Figure 1. The poloidal cross section of the computational grid used in EMC3-EIRENE for EAST modelling. The solid red circles named corners 1 and 2 mark the corners of each divertor target. The divertor targets are indicated by the orange lines. Five neon impurity injection positions and directions indicated by purple arrows are set at Upstream (U0), near the strike point at the In- and Out-board Divertors (ID0, OD0) and away from the strike point at the In- and Out-board Divertors (ID1, OD1). The purple dashed line ($R= 158.0$ cm) is used to define the boundary between the high field and low field sides of the torus for the discussion in sections 3.1.3 and 3.2.

Figure 2. The 2D distributions of heat flux deposition on the upper in- and out-board divertor targets with neon injected at U0, ID0 and OD0, respectively. The x-axis and y-axis indicate the toroidal angle and the distance between the corner and the position on the target plates, respectively. The points P1 and P2 are close to the strike points on the upper in- and out-board targets at $\varphi= 60^\circ$ and -30° , respectively.

Figure 3. The poloidal distributions of heat load on the upper in- and out-board divertor targets at the toroidal angles of $\varphi= 60^\circ$ and -120° with neon seeded at ID0 (a, b), and at the toroidal angles of $\varphi= -30^\circ$ and 150° with neon injected at OD0 (c, d). The x-axis is the distance from the location on target plates to each corner of divertor target.

Figure 4. The 2D distributions of heat load on the upper in- and out-board targets for neon injections at ID0 and OD0 with upstream electron density of $0.8 \times 10^{19} m^{-3}$ and neon injection rate of $9.38 \times 10^{20} s^{-1}$ (a, c), and $1.2 \times 10^{19} m^{-3}$ and neon injection rate of $3.13 \times 10^{20} s^{-1}$ (b, d).

Figure 5. The distributions of electron density (a) and temperature (b), neon ions density (c) and radiation power (d) along the flux tubes FT(60°) and FT(-120°) against the toroidal angle. The start points of the flux tubes FT(60°) and FT(-120°) are located at the inboard targets at the toroidal angles of $\varphi= 60^\circ$ (P1 in figure 2(b)) and -120° (the opposite toroidal location of P1), respectively.

Figure 6. The distributions of electron density (a) and temperature (b), neon ions density (c) and radiation power (d) along the flux tubes FT(-30°) and FT(150°) against the toroidal angle. The start points of the flux tubes FT(-30°) and FT(150°) are located at the outboard targets at the toroidal angles of $\varphi= -30^\circ$ (P2 in figure 2(f)) and 150° (the opposite toroidal location of P2), respectively.

Figure 7. The electron density (a) and temperature (b), neon ions density (c) and radiation power (d) along the flux tube of point P1 (i.e. FT(60°)) against the toroidal angle with neon injections at U0, ID0 and OD0. The start point P1 is located at the toroidal angle of $\varphi= 60^\circ$ on the inboard targets. When the flux tube of point P1 rotates about -3100° , the point P1 crosses the purple dashed line as shown in figure 1, i.e. migrates from the high field side to the low field side. Accordingly, the brown dashed line is used to indicate the boundary between the high field and low field sides, which is corresponding to the purple dashed line in figure 1.

Figure 8. The electron density (a) and temperature (b), neon ions density (c) and radiation power (d) along the flux tube of point P2 (i.e. FT(-30°)) against the toroidal angle with neon injections at U0, ID0 and OD0. The start point P2 is located at the toroidal angle of $\varphi = -30^\circ$ on the outboard targets. Likewise, when the flux tube of point P2 rotates about 3100°, the point P2 migrates from the low field side to the high field side.

Figure 9. The 2D distributions of heat load on the upper in- and out-board targets with neon injections at ID1 (a, c) and OD1 (b, d).

Figure 10. The electron density (a) and temperature (b), neon ions density (c) and radiation power (d) along the flux tube of point P1 (i.e. FT(60°)) against the toroidal angle with neon injections at U0, ID0 and ID1.

Figure 11. The electron density (a) and temperature (b), neon ions density (c) and radiation power (d) along the flux tube of point P2 (i.e. FT(-30°)) against the toroidal angle with neon injections at U0, OD0 and OD1.

Fig.1

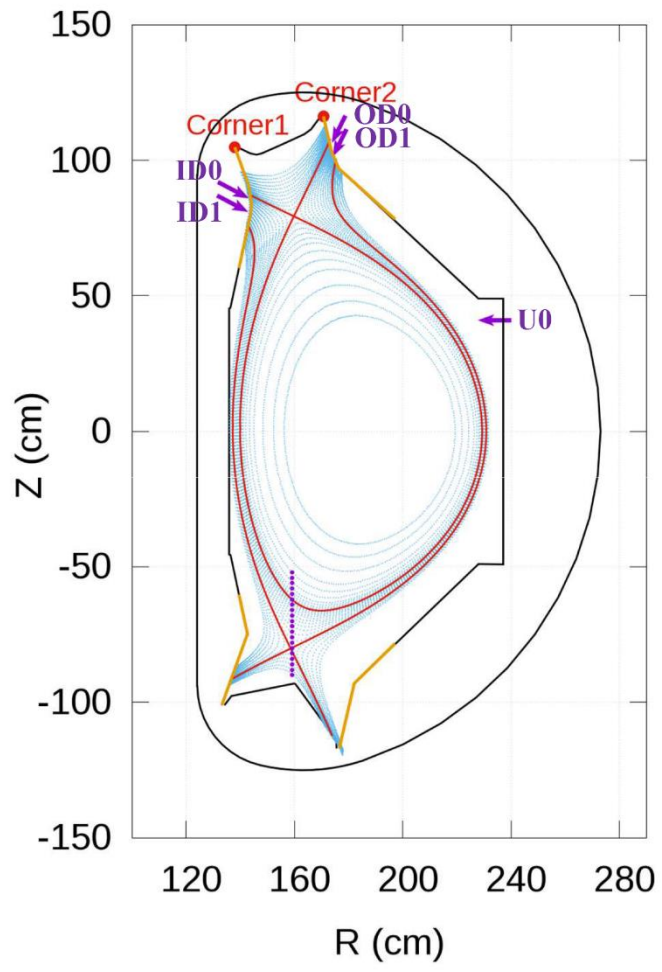


Fig 2.

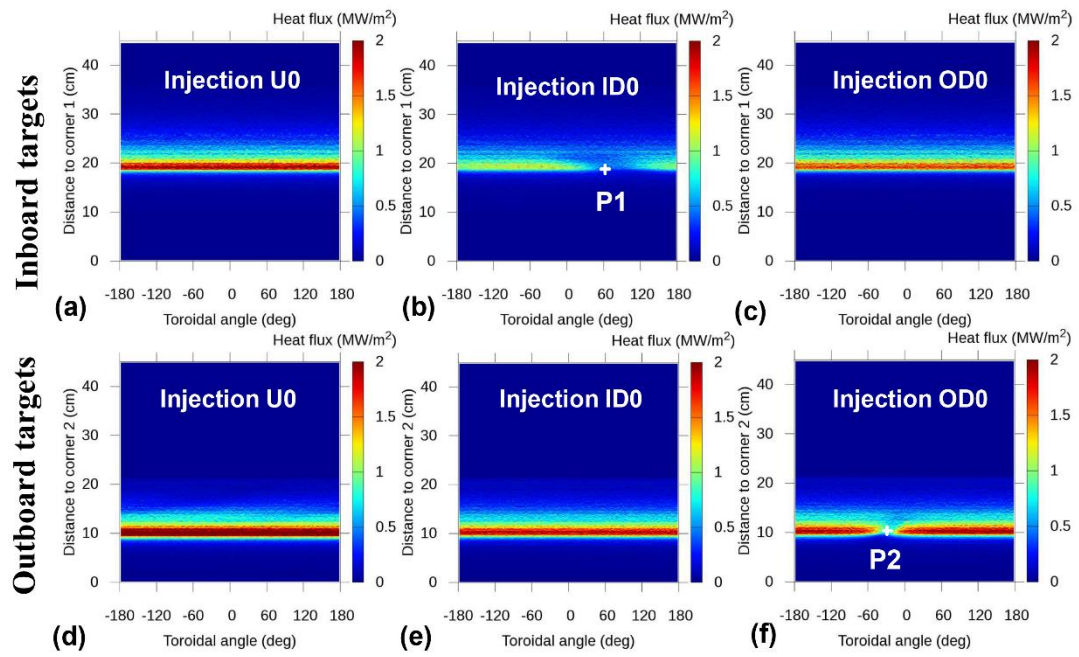


Fig 3.

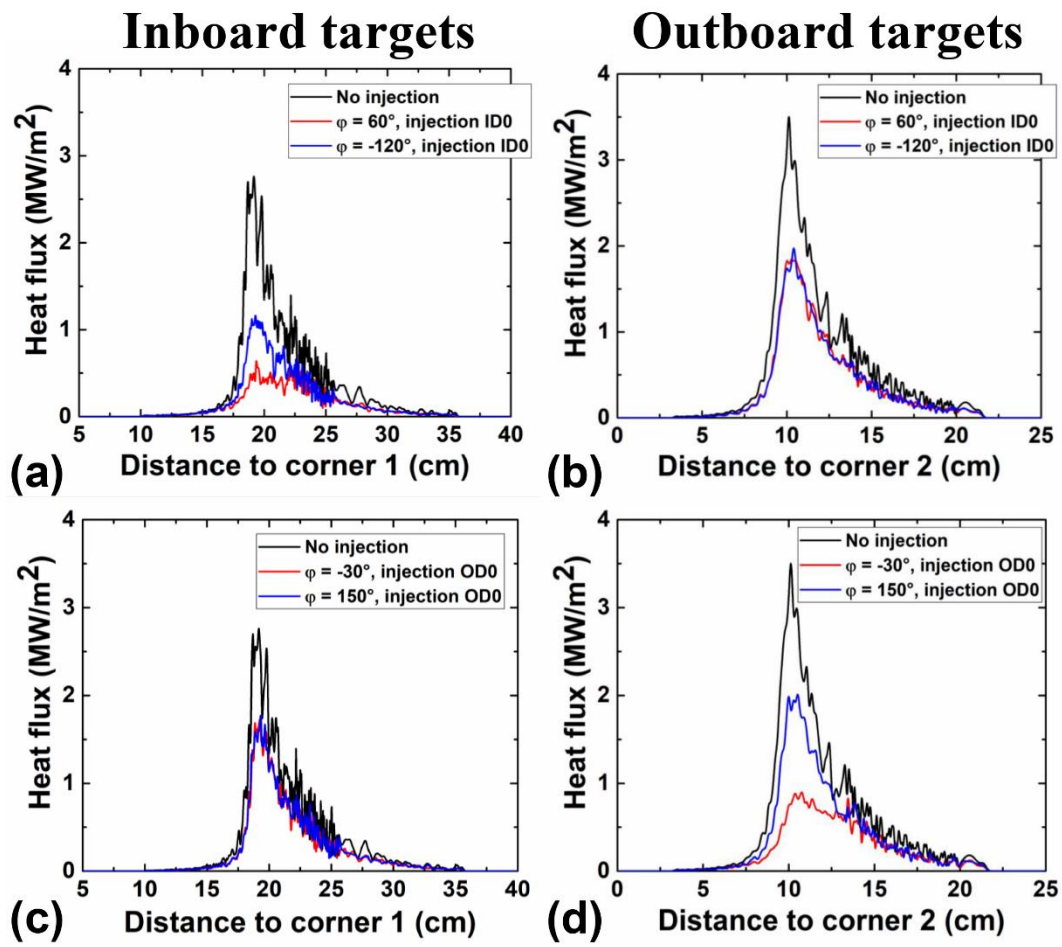


Fig 4.

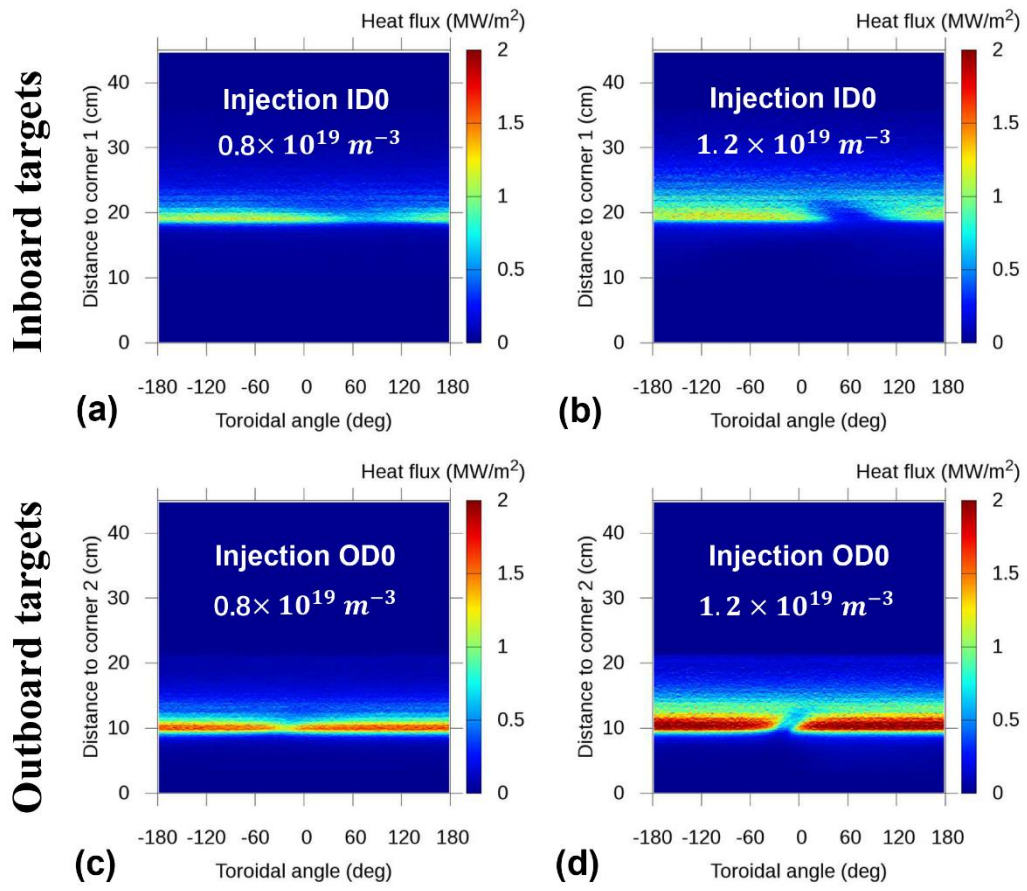


Fig 5.

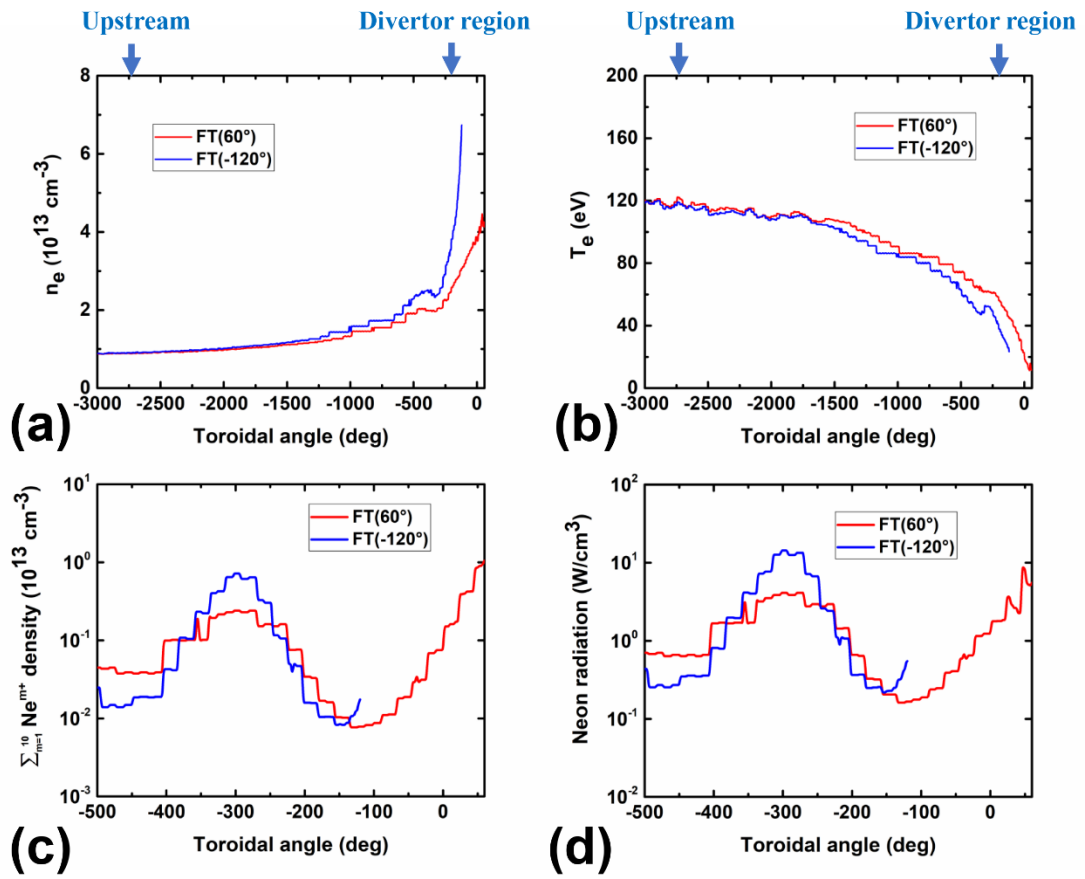


Fig 6.

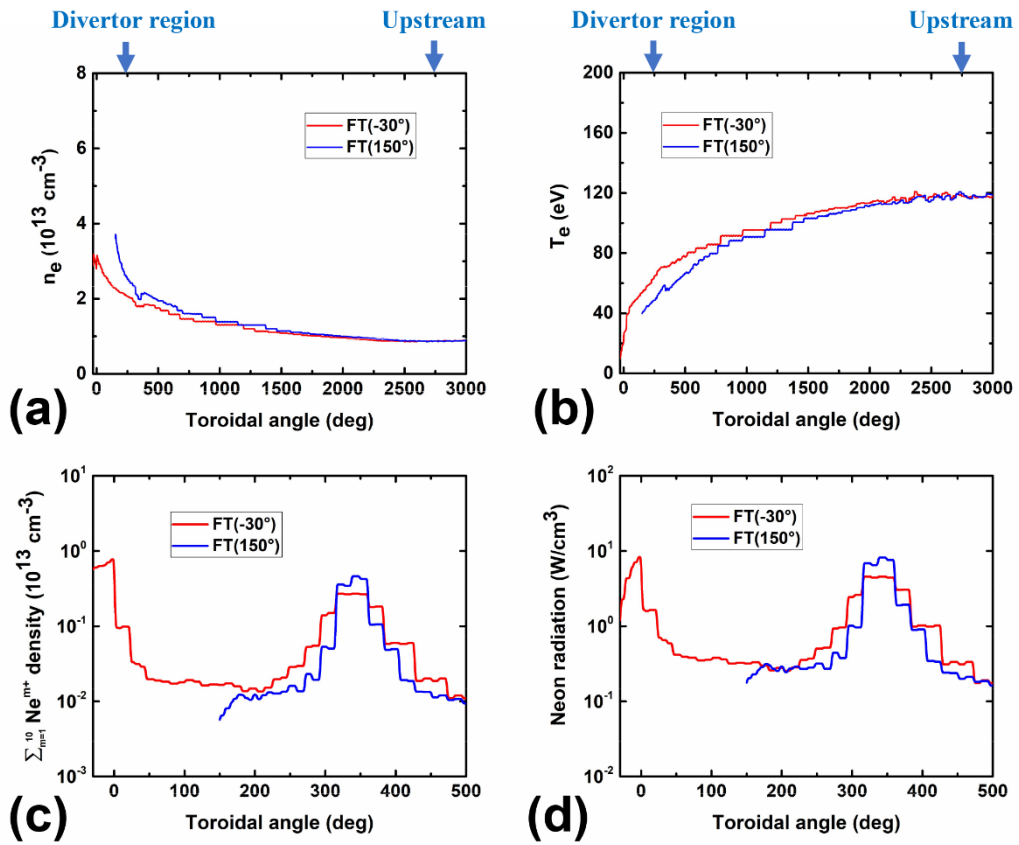


Fig 7.

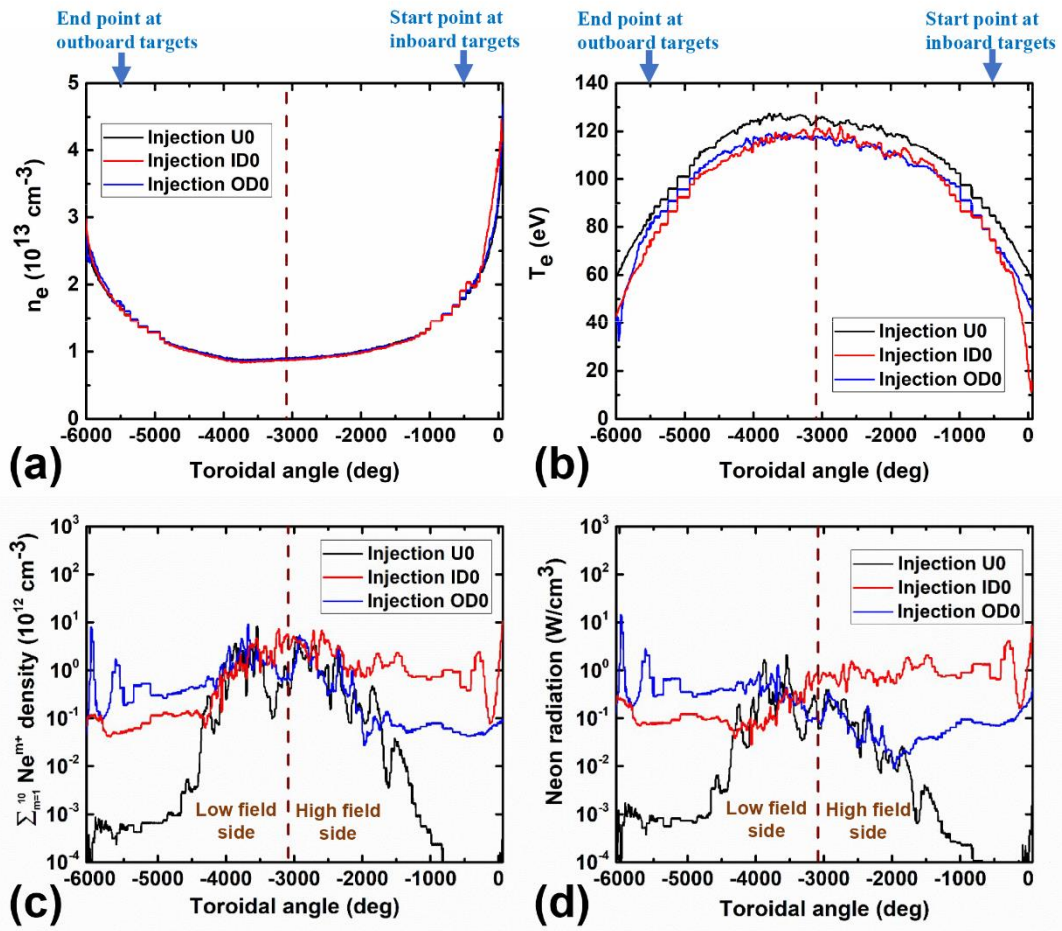


Fig 8.

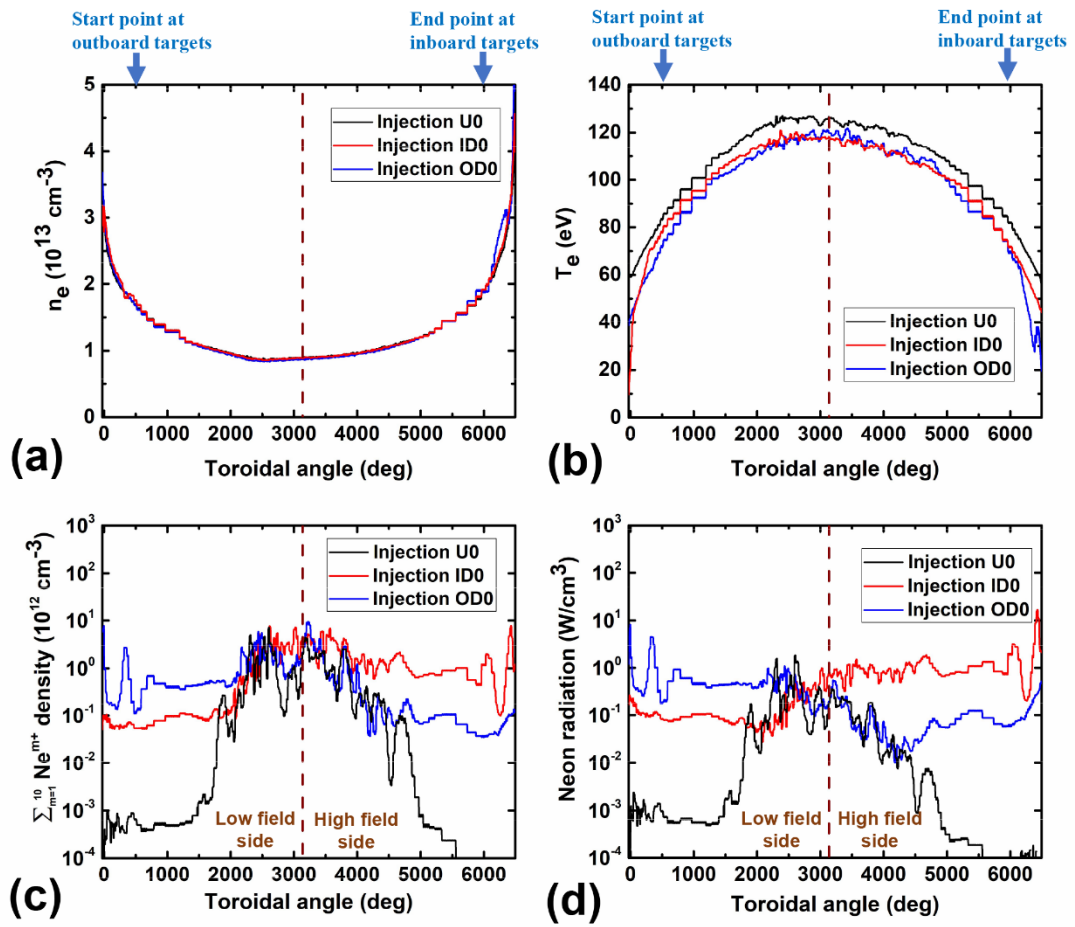


Fig 9.

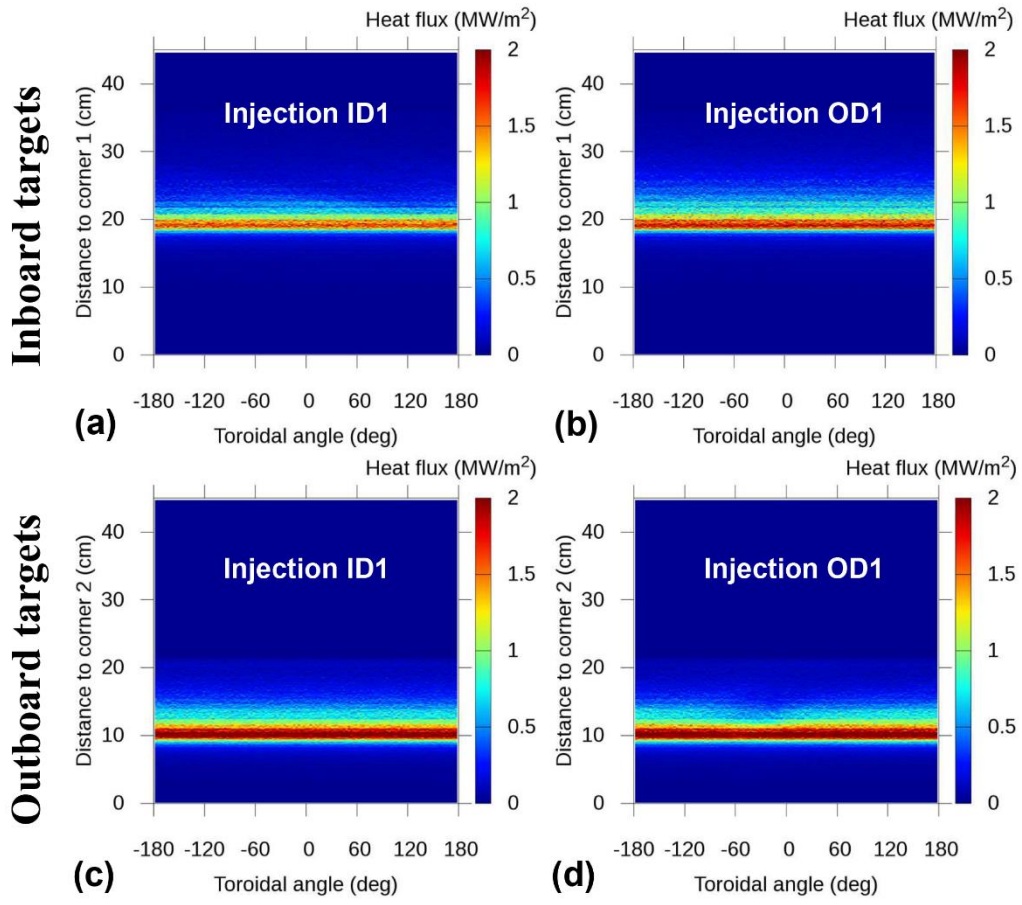


Fig 10.

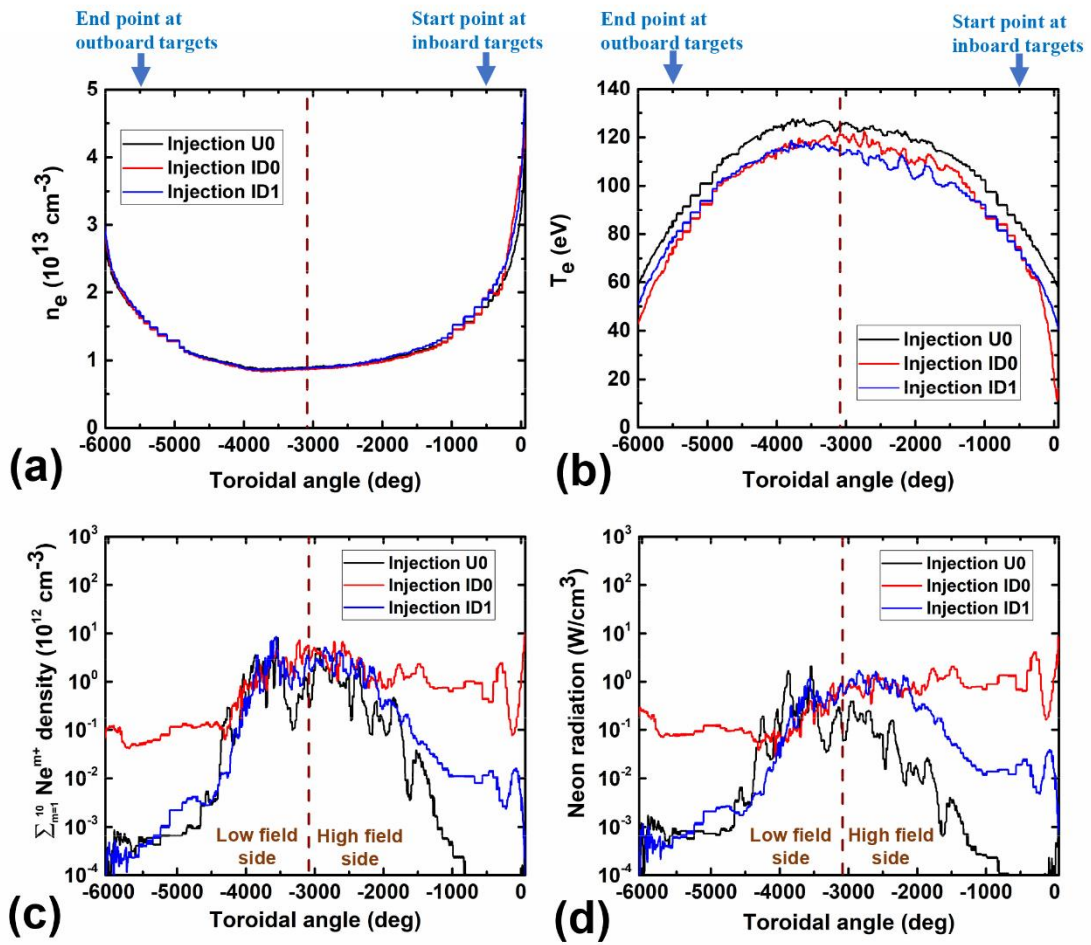


Fig 11.

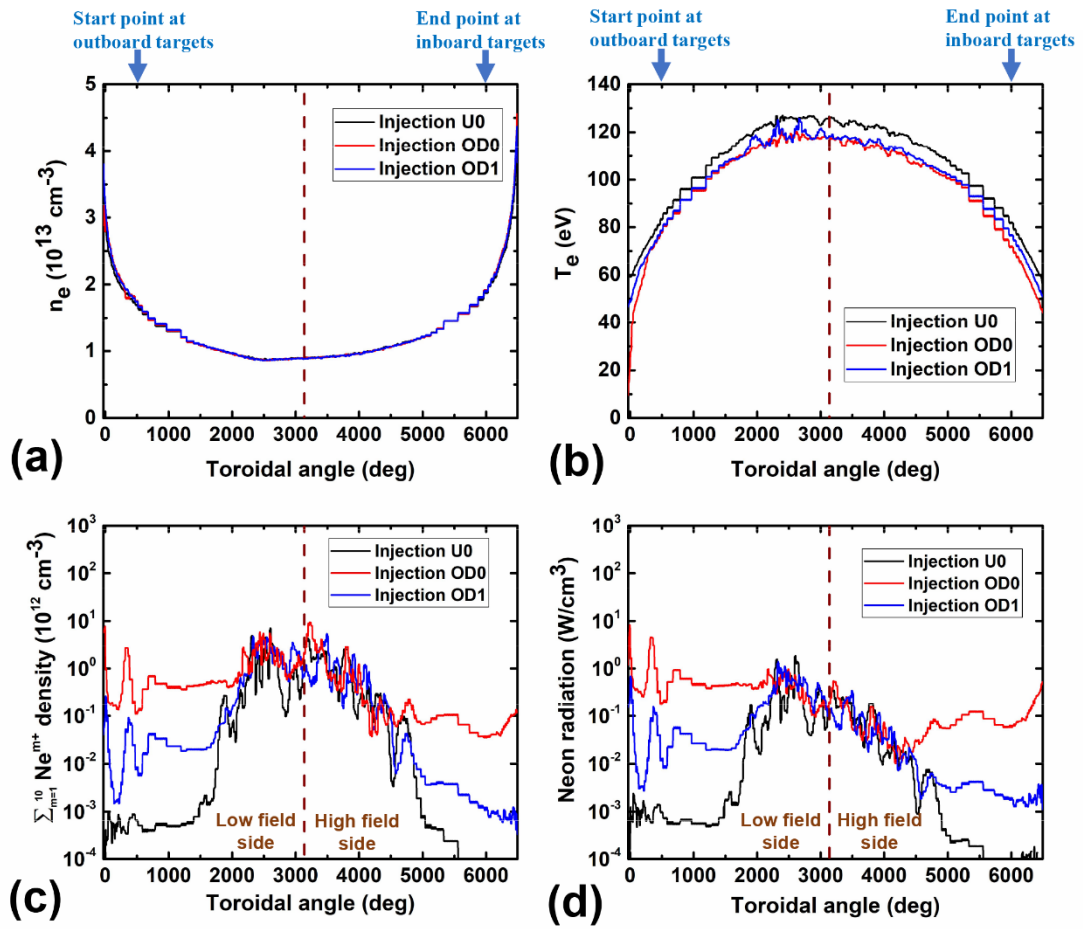


Table 1. Poloidal positions for neon injection used in the modelling.

Injection	Poloidal position (cm)
U0	R=230.0, Z=41.0
ID0	R=145.0, Z=85.0
OD0	R=173.0, Z=105.0
ID1	R=145.0, Z=80.0
OD1	R=173.0, Z=102.0